





Prebiotic Precursors of the Primordial RNA World in Space: Detection of NH₂OH

Víctor M. Rivilla^{1,2} , Jesús Martín-Pintado¹, Izaskun Jiménez-Serra¹, Sergio Martín^{3,4} , Lucas F. Rodríguez-Almeida¹, Miguel A. Requena-Torres^{5,6}, Fernando Rico-Villas¹, Shaoshan Zeng⁷, and Carlos Briones¹

¹Centro de Astrobiología (CSIC-INTA), Ctra. de Ajalvir Km. 4, Torrejón de Ardoz, E-28850 Madrid, Spain

²INAF-Osservatorio Astrofisico di Arcetri, Largo Enrico Fermi 5, I-50125, Florence, Italy

³European Southern Observatory, Alonso de Córdova 3107, Vitacura Casilla 763 0355, Santiago, Chile

⁴Joint ALMA Observatory, Alonso de Córdova 3107, Vitacura 763 0355, Santiago, Chile

⁵University of Maryland, College Park, ND 20742-2421, USA

⁶Department of Physics, Astronomy and Geosciences, Towson University, Towson, MD 21252, USA

⁷Star and Planet Formation Laboratory, Cluster for Pioneering Research, RIKEN, 2-1 Hirosawa, Wako, Saitama, 351-0198, Japan

Received 2020 May 25; revised 2020 July 29; accepted 2020 July 31; published 2020 August 19

Abstract

One of the proposed scenarios for the origin of life is the primordial RNA world, which considers that RNA molecules were likely responsible for the storage of genetic information and the catalysis of biochemical reactions in primitive cells, before the advent of proteins and DNA. In the last decade, experiments in the field of prebiotic chemistry have shown that RNA nucleotides can be synthesized from relatively simple molecular precursors, most of which have been found in space. An important exception is hydroxylamine, NH₂OH, which, despite several observational attempts, it has not been detected in space yet. Here we present the first detection of NH₂OH in the interstellar medium toward the quiescent molecular cloud G+0.693-0.027 located in the Galactic Center. We have targeted the three groups of transitions from the $J = 2-1$, $3-2$, and $4-3$ rotational lines, detecting five transitions that are unblended or only slightly blended. The derived molecular abundance of NH₂OH is $(2.1 \pm 0.9) \times 10^{-10}$. From the comparison of the derived abundance of NH₂OH and chemically related species, with those predicted by chemical models and measured in laboratory experiments, we favor the formation of NH₂OH in the interstellar medium via hydrogenation of NO on dust grain surfaces, with possibly a contribution of ice-mantle NH₃ oxidation processes. Further laboratory studies and quantum chemical calculations are needed to completely rule out the formation of NH₂OH in the gas phase.

Unified Astronomy Thesaurus concepts: [Pre-biotic astrochemistry \(2079\)](#); [Astrochemistry \(75\)](#); [Astrobiology \(74\)](#); [Interstellar molecules \(849\)](#); [Galactic center \(565\)](#)

Supporting material: data behind figure

1. Introduction

Life likely appeared about 3.8 billion years ago, 700 Myr after the formation of the Earth (Mojzsis et al. 1996). However, the processes that allowed the transition from chemistry to biology are still uncertain. Present-day life is mainly based on three biopolymers: RNA and DNA nucleic acids, which store genetic information, and proteins, responsible for most metabolic activities. One of the main challenges for understanding the origin of life is the “chicken and egg” paradox: nucleic acids need catalytic proteins for their replication, while the biosynthesis of proteins requires the prior presence of genetic information coded in nucleic acids. To solve this problem, Gilbert (1986) proposed the hypothesis of a primordial RNA world, in which RNA molecules could have performed the functions that were carried out by DNA and proteins in the subsequent DNA/RNA/protein world.

One of the weaknesses of the RNA world hypothesis was that ribonucleotides (RNA monomers) seemed unlikely to be synthesized under plausible prebiotic conditions (Atkins et al. 2011; Ruiz-Mirazo et al. 2014). However, this possibility has recently gained support thanks to prebiotic chemistry experiments that have shown that ribonucleotides can be formed from relatively simple organic molecules such as cyanoacetylene (HC₃N), cyanamide (NH₂CN), glycolaldehyde (CH₂OHCHO), urea (NH₂CONH₂) and/or hydroxylamine (NH₂OH; see Powner 2009; Patel 2015; Becker et al. 2016, 2019).

Interestingly, except for NH₂OH, all these RNA molecular precursors have been detected in the interstellar medium (ISM; Turner 1971; Turner et al. 1975; Hollis et al. 2000;

Belloche et al. 2019). As recently shown by Becker et al. (2019), NH₂OH is a key precursor in the unified synthesis of both pyrimidine and purine ribonucleotides. However, observational searches of NH₂OH in the ISM have so far been unsuccessful (Pulliam et al. 2012; McGuire et al. 2015; Ligterink et al. 2018). This is a puzzling result since NH₂OH is expected to form efficiently on dust grains according to chemical models and laboratory experiments (Garrod et al. 2008; Zheng & Kaiser 2010; Fedoseev et al. 2012; Garrod 2013; He et al. 2015).

In this Letter, we present the first detection of NH₂OH in the ISM toward the quiescent molecular cloud G+0.693-0.027 (G+0.693, hereafter) located in the Sgr B2 complex in the Galactic Center. This cloud shows very rich chemistry in complex organic molecules (Martín et al. 2008; Requena-Torres et al. 2008; Rivilla et al. 2018, 2019; Zeng et al. 2018), including urea (Jiménez-Serra et al. 2020), another key ingredient in the pathway to ribonucleotides proposed by Becker et al. (2019). All this makes G+0.693 the perfect target to search for NH₂OH in the ISM.

2. Observations

We have carried out a high-sensitivity spectral survey at 3, 2, and 1 mm toward the G+0.693 molecular cloud using the IRAM 30 m telescope. The IRAM 30 m observations were performed in three observing runs during 2019: April 10–16, August 13–19, and December 11–15 (projects numbers 172-18, 018-19 and 133-19). We used the broadband Eight MIXer Receiver and the fast Fourier transform spectrometers in FTS200 mode, which provided a

Table 1
List of Observed Transitions of NH₂OH

Frequency (GHz)	Transition (J_{K_a, K_c})	$\log I$ (nm ² MHz)	$S_{ul} \times \mu^2$ (D ²)	$\log A_{ul}$ (s ⁻¹)	g_u	E_u (K)	Blending ^a
100.683580	2 _{1,2} –1 _{1,1}	–4.8754	0.52036	–5.9078	5	15.2	blended with CH ₃ OCHO
100.748230	2 _{0,2} –1 _{0,1}	–4.7384	0.69380	–5.7821	5	7.2	unblended
100.807620	2 _{1,1} –1 _{1,0}	–4.8743	0.52041	–5.9062	5	15.2	blended with CH ₃ COOH and s-C ₂ H ₅ CHO
151.020701	3 _{1,3} –2 _{1,2}	–4.2821	0.92509	–5.2759	7	22.4	unblended
151.101986	3 _{2,2} –2 _{2,1}	–4.5203	0.57820	–5.4793	7	46.3	blended with s-C ₂ H ₅ CHO
151.102324	3 _{2,1} –2 _{2,0}	–4.5203	0.57820	–5.4793	7	46.3	blended with s-C ₂ H ₅ CHO
151.117668	3 _{0,3} –2 _{0,2}	–4.2189	1.04068	–5.2239	7	14.5	slightly blended with s-C ₂ H ₅ CHO ^b
151.207007	3 _{1,2} –2 _{1,1}	–4.2810	0.92520	–5.2742	7	22.5	slightly blended with unidentified line
201.352578	4 _{1,4} –3 _{1,3}	–3.8964	1.30100	–4.8621	9	32.1	blended with CH ₃ SH and HDCO
201.435072	4 _{3,2} –3 _{3,1}	–4.3192	0.60710	–5.1926	9	95.8	blended with CH ₃ OH
201.435072	4 _{3,1} –3 _{3,0}	–4.3192	0.60710	–5.1926	9	95.8	blended with CH ₃ OH
201.460663	4 _{2,3} –3 _{2,2}	–4.0274	1.04082	–4.9584	9	56.0	blended with CH ₃ OH
201.461598	4 _{2,2} –3 _{2,1}	–4.0274	1.04081	–4.9583	9	24.1	blended with CH ₃ OH
201.481718	4 _{0,4} –3 _{0,3}	–3.8563	1.38777	–4.8333	9	32.1	slightly blended with unidentified line
201.600715	4 _{1,3} –3 _{1,2}	–3.8954	1.30089	–4.8606	9	15.6	blended with H ₂ C ¹⁸ O and CH ₃ CONH ₂

Notes. We provide the parameters from CDMS catalog entry 33503: frequencies, quantum numbers, base 10 logarithm of the integrated intensity at 300 K ($\log I$), and upper state degeneracy (g_u). We also show the values of $S_{ul} \times \mu^2$, the base 10 logarithm of the Einstein coefficients ($\log A_{ul}$), and the energy of the upper levels (E_u). The last column gives the information about the species with transitions blending with some of the NH₂OH lines.

^a Detailed information about the species producing some blending is presented in Appendix A (Table A1).

^b The analysis of s-propanal (s-C₂H₅CHO) is presented in Appendix B.

channel width of ~ 200 kHz, i.e., a velocity resolution of ~ 0.3 – 0.85 km s⁻¹. We smoothed the spectra to resolutions of 1.6, 1.4, and 4.0 km s⁻¹ for the 3, 2, and 1 mm data, respectively, high enough to sample the observed line widths of ~ 15 – 25 km s⁻¹, and to provide similar rms noise (2.6–3.8 mK), and optimal line visualization. We stress that the results of our analysis (described in Section 3) are independent of the spectral resolution. Each frequency setup was observed several times, with the central frequency shifted by 20–100 MHz in order to identify possible spectral features resulting from unsuppressed image side-band emission. The image-band lines, identified by comparing the same frequency range observed during two different spectral setups, were eliminated during the reduction of the data. The covered spectral ranges were 71.76–116.72 GHz, 124.77–175.5 GHz, 199.8–238.29 GHz, 252.52–260.30 GHz, and 268.2–275.98 GHz. The observations were centered at $\alpha(J2000.0) = 17^{\text{h}}47^{\text{m}}22^{\text{s}}$, $\delta(J2000.0) = -28^{\circ}21'27''$. The position switching mode was used in all observations, with the off position located at ($-885''$, $290''$) from the source position. The intensity of the spectra is given in T_A^* , as the molecular emission toward G+0.693 is relatively extended over the beam (Requena-Torres et al. 2006; Rivilla et al. 2018).

3. Analysis and Results

The identification of the molecular lines was performed using version 2020 June 19 of the Spectral Line Identification and Modeling (SLIM) tool within the MADCUBA package⁸ (Martín et al. 2019), which uses the spectroscopic entries from the Cologne Database for Molecular Spectroscopy (CDMS, Endres et al. 2016) and the Jet Propulsion Laboratory (JPL; Pickett et al. 1998), and generates the synthetic spectra under the assumption of local thermodynamic equilibrium (LTE) conditions. The spectroscopic information of NH₂OH (CDMS entry 33503, from 2003 March) was obtained from Tsunekawa

(1972) and Morino et al. (2000). NH₂OH is nearly a prolate symmetric top molecule, in which the principal a - and c -axes are in a plane of symmetry. Both a -type ($\Delta K_a = 0$) and c -type ($\Delta K_c = 0$) transitions are allowed, but only the former are expected to be detected in the ISM since the projected dipole moment along the a -axis is about 10 times larger (Tsunekawa 1972). The partition function of the ground vibrational state used in the analysis, obtained from the CDMS entry, does not have a substantial contribution from the lowest-lying vibrational states (with energies >555 K, Morino et al. 2000) due to the low excitation temperatures of the molecular emission toward G+0.693 ($T_{\text{ex}} \sim 5$ – 20 K; Requena-Torres et al. 2008; Zeng et al. 2018; Rivilla et al. 2019).

We list in Table 1 all the a -type transitions of NH₂OH that fall in the observed data: 15 lines of the rotational transitions $J = 2-1$, $3-2$, and $4-3$. We note that transitions from higher energy levels ($J_u > 5$) have low predicted intensities due to the low excitation temperatures of G+0.693. The fitted line profiles of NH₂OH (see details of the fit below) are shown with a red solid line in the left panels of Figure 1. Five of the targeted NH₂OH transitions (1 at 3 mm, 3 at 2 mm, and 1 at 1 mm, indicated with an asterisk in Figure 1), appear either unblended or only slightly blended. The other transitions, which are blended with brighter lines from other molecules, have predicted intensities consistent with the observed spectra.

To properly evaluate the line contamination by other molecules we have searched for more than 300 different molecules in our data set, including all the species detected previously toward G+0.693 (e.g., Requena-Torres et al. 2006, 2008; Rivilla et al. 2018, 2019; Zeng et al. 2018; Jiménez-Serra et al. 2020), and those detected so far in the ISM (McGuire 2018).⁹ We have fitted the emission of all the detected molecules, and produced the total LTE spectra, which is shown with a solid blue line in the left panels of Figure 1. We list in the last column of Table 1

⁸ Madrid Data Cube Analysis on ImageJ is a software developed at the Center of Astrobiology (CAB) in Madrid; <http://cab.inta-csic.es/madcuba/Portada.html>.

⁹ See also <https://cdms.astro.uni-koeln.de/classic/molecules>, and http://astrochymist.org/astrochymist_mole.html.

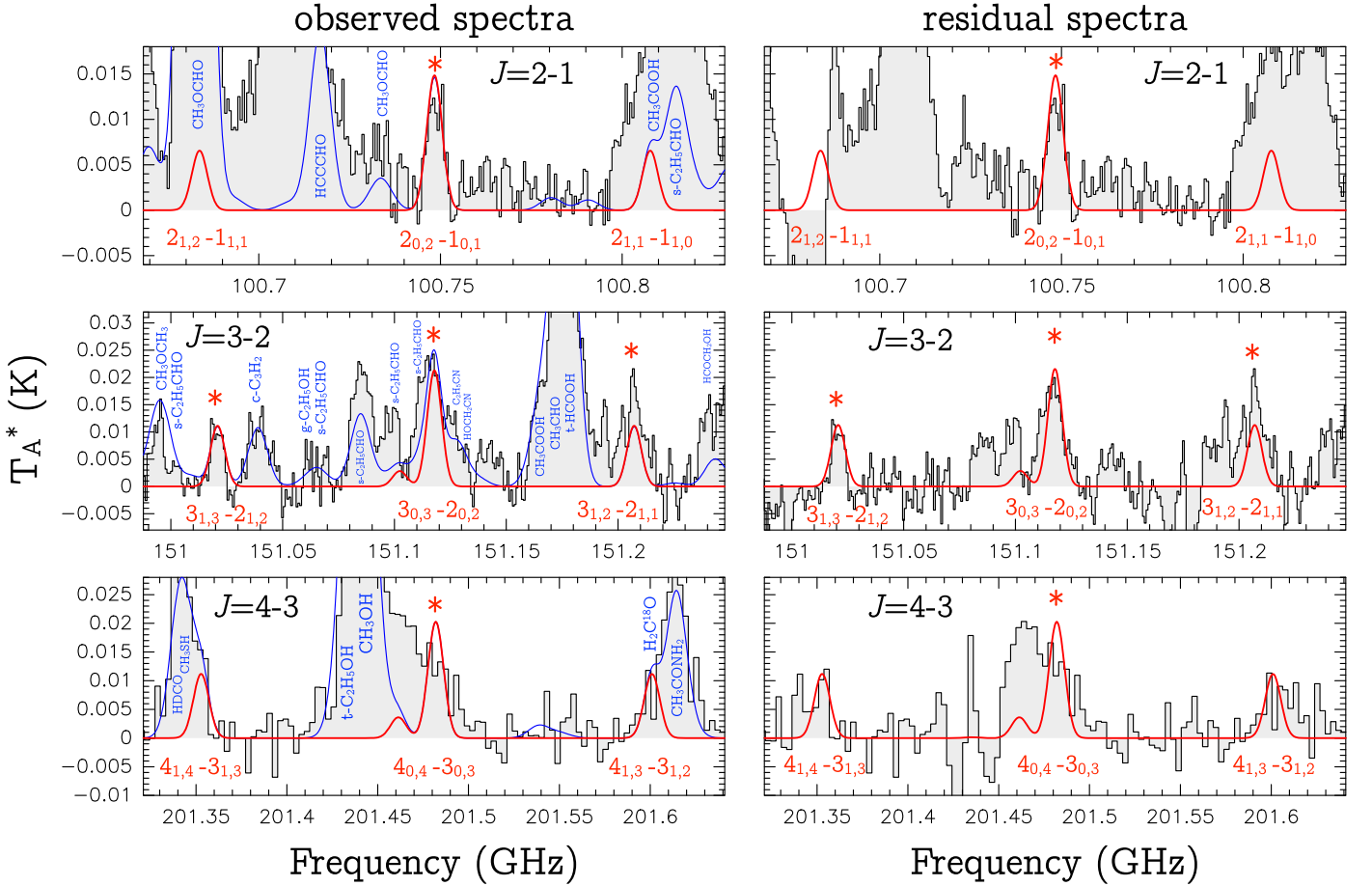


Figure 1. Left panels: transitions of NH_2OH detected in the observed spectra of G+0.693. The nine brightest transitions are labeled with their quantum numbers. The five transitions that are unblended or only slightly blended are indicated with red asterisks. The best LTE fit to the NH_2OH lines is shown in red, while the total contribution, including other molecular species (labeled) identified in the region is shown in blue. Right panels: residual spectra resulting from subtracting the LTE modeled contribution of all other identified molecular species except NH_2OH from the observed spectra. The best LTE fit to the NH_2OH lines is shown in red.

(The data used to create this figure are available.)

the molecules with transitions that produce blending with some of the NH_2OH lines. More detailed information about all the identified molecular transitions that contribute to the line emission in the spectral ranges shown in Figure 1 is presented in Appendix A.

To highlight the emission from NH_2OH , we have computed the residual spectra obtained by subtracting from the observed spectra the predicted LTE contribution for all the identified molecular species but NH_2OH . The resulting residual spectra, shown in the right panels of Figure 1, clearly exhibit the spectral line profiles that match the LTE predictions for NH_2OH in red solid lines (see below), supporting the identification of NH_2OH .¹⁰

To derive the physical parameters that explain the NH_2OH emission, we used the SLIM-AUTOFIT tool of MADCUBA, which provides the best nonlinear least-squares LTE fit to the data using the Levenberg–Marquardt algorithm. The fitted parameters are molecular column density (N), excitation temperature (T_{ex}), central velocity (v_{LSR}), and FWHM of the Gaussian profiles. SLIM considers the solution of the radiative transfer as described in Equation (4) of Martín et al. (2019). For the modeling of G+0.693, where no continuum emission is detected (e.g., Ginsburg et al. 2016), we consider $T_c = 0$, and the cosmic background

temperature of $T_{\text{bg}} = 2.73$ K. The fit to the NH_2OH profiles was performed by also considering the total contribution of the LTE emission from all the other identified molecules (blue line in Figure 1). We fixed the line width to 15 km s^{-1} , which reproduces the profiles of the two strongest completely unblended transitions, $2_{0,2}-1_{0,1}$ and $3_{1,3}-2_{1,2}$ (Figure 1). This value is consistent with the typical molecular line widths found toward G+0.693, which span between 14 and 34 km s^{-1} (e.g., Requena-Torres et al. 2008; Zeng et al. 2018). We considered typical values of T_{ex} found in G+0.693 in the range 5–20 K (see e.g., Zeng et al. 2018). Low values (5–10 K) underestimate the observed intensities of the NH_2OH transitions at 2 and 1 mm, while values in the range 15–20 K are able to reproduce well all the transitions. We thus fixed $T_{\text{ex}} = 15 \text{ K}$ ¹¹ to perform the fit, noting that if the assumed fixed value is 20 K the derived column density would only vary by a factor of ~ 1.1 . We then performed AUTOFIT, leaving column density and v_{LSR} as free parameters. The resulting best LTE fit is shown by the red curve in Figure 1, and the derived physical parameters are presented in Table 2. To derive the final uncertainty of the column density we added quadratically the error derived from the fitting algorithm, and 20% from the typical flux density uncertainty of the IRAM 30 m telescope.

¹⁰ We note that the NH_2OH transition at 100.683580 GHz is not well reproduced in the residual spectra due to the oversubtraction of the LTE model of two bright contaminating transitions of CH_3OCH_3 : $9_{0,9}-8_{0,8}$ A and E.

¹¹ The value of the partition function of NH_2OH , $\log Q(15 \text{ K}) = 1.4613$, is obtained by log–log linear interpolation of the values at 9.375 and 18.75 K from CDMS.

Table 2
Derived Physical Parameters of NH₂OH and Other Molecular Species That Might be Chemically Related

Molecule	N ($\times 10^{13}$ cm ⁻²)	T_{ex} (K)	v_{LSR} (km s ⁻¹)	FWHM (km s ⁻¹)	Abundance ^a ($\times 10^{-10}$)	Reference
NH ₂ OH	2.8 ± 0.6	15	68.6 ± 0.8	15	2.1 ± 0.9	1
HNO	5.8 ± 1.3	3.7 ± 0.2	66.4 ± 0.4	20.5 ± 0.9	4.3 ± 1.8	1
N ₂ O	48 ± 11	18 ± 2	64.7 ± 0.8	21 ± 2	36 ± 15	1
NO	3600 ± 200	4.1 ± 0.4	68 ± 1	21 ± 1	2700 ± 700	2
NO ₂	<29	10	69	20	<22	1
HONO	<0.2	10	69	20	<0.16	1
HNO ₃	<0.5	10	69	20	<0.33	1

Notes.

^a We adopted $N_{\text{H}_2} = (1.4 \pm 0.3) \times 10^{23}$ cm⁻², from Martín et al. (2008).

References. (1) This work, (2) Zeng et al. (2018).

Table 3
Molecular Abundances and Molecular Abundances Ratios

Region	NH ₂ OH	NO	N ₂ O	NH ₂ OH/NO	NO/N ₂ O	References
G+0.693	2.1×10^{-10}	2.7×10^{-7}	3.5×10^{-9}	$\sim 8 \times 10^{-4}$	76	1
L1157-B1	$<1.4 \times 10^{-8}$	$(4-7) \times 10^{-6}$...	$<3 \times 10^{-3}$...	2,3
IRAS 16293-2422 B	$<3.1 \times 10^{-11}$	1.7×10^{-9}	3.3×10^{-9}	$<2 \times 10^{-2}$	0.5	4
Sgr B2(N) ^a	$<8 \times 10^{-12}$	6.2×10^{-9}	1.5×10^{-9}	$<1.3 \times 10^{-3}$	4	5,6
Sgr B2(M)	...	9×10^{-9}	1×10^{-9}	...	9	7

Note.

^a For a comparison with the NH₂OH upper limit obtained by Pulliam et al. (2012), the NO abundance has been recalculated using the column density reported by Halfen et al. (2001) and the hydrogen column density used by Pulliam et al. (2012).

References. (1) This work, (2) McGuire et al. (2015), (3) Codella et al. (2018), (4) Ligterink et al. (2018), (5) Pulliam et al. (2012), (6) Halfen et al. (2001), (7) Ziurys et al. (1994).

We obtain a column density of $(2.8 \pm 0.6) \times 10^{13}$ cm⁻², which translates to a molecular abundance with respect to molecular hydrogen of $(2.1 \pm 0.9) \times 10^{-10}$.

To gain insight into the interstellar chemistry and synthesis routes of NH₂OH in the ISM, we have also analyzed the emission from chemically related species. We detected the nitroxyl radical (HNO) and nitrous oxide (N₂O). The observed spectra along with the derived best LTE fits for these two molecules, reported for the first time in G+0.693 in this Letter, are presented in Appendix C. Other species, such as HONO, NO₂, and HNO₃, were not detected. The derived physical parameters for all these species are reported in Table 2.

4. Discussion

4.1. Formation of NH₂OH in the ISM

Table 3 compares the abundance of NH₂OH in G+0.693 with the upper limits found in other regions where it has been previously searched for. We find that the abundance of NH₂OH in G+0.693 is about a factor of 6 and 25 higher than the upper limits measured in the hot corino IRAS 16293–2422 B and the hot core Sgr B2(N), respectively (Pulliam et al. 2012; Ligterink et al. 2018). Unfortunately, the upper limit toward the protostellar shock L1157-B1 (McGuire et al. 2015) is too high for a meaningful comparison.

The several routes that have been proposed for the synthesis of NH₂OH in the ISM, all of them based on surface chemistry, are summarized in Table 4. The hydrogenation of nitrogen oxide (NO) (Route 1; Table 4) was suggested theoretically by Charnley et al. (2001) and it has been confirmed experimentally by different groups (Congiu et al. 2012; Fedoseev et al. 2012). In this process, the successive hydrogenation of NO and its products HNO and

Table 4
Grain-surface Routes Proposed for the Formation of NH₂OH

	Route	References
(1)	NO → HNO → H ₂ NO/HNOH → NH ₂ OH	i
(2a)	NH ₂ + H+H ₂ O → NH ₂ OH + H ₂	ii
(2b)	NH ₂ + OH → NH ₂ OH	iii
(3)	NH ₃ + O → NH ₂ OH	iv
(4)	NH ₃ + O ₂ → NH ₂ OH + O	v

References. (i) Fedoseev et al. (2012), Congiu et al. (2012), (ii) Nishi et al. (1984), (iii) Nishi et al. (1984), Zheng & Kaiser (2010), (iv) He et al. (2015), (v) Tsegaw et al. (2017).

H₂NO, is barrierless (or it occurs with very small activation barriers), yielding NH₂OH in a very efficient way even at low temperatures (Congiu et al. 2012; Fedoseev et al. 2012). This chemical scheme requires the presence of significant amounts of NO on grain surfaces. For the case of G+0.693, this is not an issue, since high abundances of this molecule are measured toward this source (of $\sim 3 \times 10^{-7}$; Table 3). Similar high abundances of NO have been measured toward the shocked region B1 in the L1157 molecular outflow (Codella et al. 2018, Table 3). These authors showed that such high NO abundance can be produced via the neutral-neutral reaction N + OH → NO + H in the gas phase. Thus, a significant fraction of NO would then be available to deplete onto dust grains at the low dust temperatures of G+0.693 ($T \leq 30$ K; Rodríguez-Fernández et al. 2004).

Although NO could be destroyed prior to being depleted onto dust grains due to its conversion to N₂O via the gas-phase reaction NO + NH → N₂O + H (Halfen et al. 2001), this mechanism does

not seem efficient in G+0.693, where the NO/N₂O ratio of 76 is much higher than those found in hotter sources (Table 3). As indicated by Halfen et al. (2001), this gas-phase reaction is only efficient for kinetic temperatures >150 K. The gas kinetic temperature in G+0.693 is 50–120 K (Hüettemeister et al. 1993; Krieger et al. 2017), i.e., lower than that in hot cores/corinos (with temperatures of 200–300 K; Belloche et al. 2013; Jørgensen et al. 2016), which would explain the low efficiency of the gas-phase conversion of NO into N₂O. Note, however, that N₂O could also be formed on the surface of dust grains (Congiu et al. 2012; Fedoseev et al. 2012), and be subsequently desorbed by shocks in G+0.693, which might explain the observed N₂O.

In addition, we have also detected HNO (see Table 2 and Appendix C), the first hydrogenation product of NO, supporting this chemical route. Although several gas-phase formation routes of HNO exist, such as, e.g., NH₂ + O → H + HNO, or HCO + NO → HNO + CO (see the KIDA database,¹² Wakelam et al. 2012), Hasegawa et al. (1992) showed that the predicted abundance of HNO in models that consider only gas-phase reactions is of just a few 10⁻¹¹. Since the derived abundance of HNO in G+0.693 is about one order of magnitude higher, the formation of HNO in G+0.693 likely occurs mainly on the surface of dust grains through the NO hydrogenation chain that also produces NH₂OH.

Other NH₂OH formation pathways have been proposed by laboratory experiments (Nishi et al. 1984; Zheng & Kaiser 2010) and chemical modeling (Garrod 2013) involving the amidogen radical NH₂ (see Routes 2a and 2b in Table 4). However, we note again that the low dust temperature in G+0.693 ($T \leq 30$ K, Rodríguez-Fernández et al. 2004) would limit the mobility of heavier radicals such as NH₂ or OH on grain surfaces (Routes 2a and 2b) compared to atomic H (Route 1), which suggests that the hydrogenation route is more plausible.

The third grain-surface reaction for the formation of NH₂OH is the oxidation of NH₃ (Routes 3 and 4 in Table 4). The experiments of He et al. (2015) and Tsegaw et al. (2017) show that NH₂OH can be formed on the surface of dust grains from NH₃ and O/O₂ at warm (~70 K) and cold temperatures (<10 K), respectively. In the He et al. (2015) work, however, the predicted ice-mantle abundance of NH₂OH (with respect to H) lies in the range 10⁻⁵–10⁻⁶, which is several orders of magnitude higher than the one observed in the gas phase of G+0.693. In addition to missing destruction pathways, this could be due to an optimistic value of the reaction rate of NH₃ + O → NH₂OH in He et al. (2015), since the oxidation of NH₃ in their experiments occurs via the Eley–Rideal mechanism, which may be more efficient than the Langmuir–Hinschelwood mechanism taking place on interstellar dust grains.

The second oxidation route, NH₃ + O₂ → NH₂OH + O, has been studied by the laboratory experiments by Tsegaw et al. (2017), in which interstellar ice analogs were irradiated with energetic electrons to mimic the effect of cosmic rays. Since G+0.693 is affected by a high cosmic-ray ionization rate (Requena-Torres et al. 2006; Zeng et al. 2018), this oxidation route might be a possible additional mechanism for the formation of NH₂OH.

In contrast to grain-surface chemistry, very little is known about possible gas-phase formation routes for NH₂OH. Experimental works have shown that gas-phase production of NH₂OH through the reaction between HNO⁺ and H₂, is inefficient (Blagojevic et al. 2003). Neutral–neutral reactions such as NH₃ + OH or NH₂ + OH are expected to be efficient at the kinetic temperatures of

G+0.693 (see KIDA database). However, these reactions mainly yield, respectively, NH₂ + H₂O and NH + H₂O. Indeed, no NH₂OH seems to be found in the products of the gas-phase reaction NH₃ + H₂O (D. Heard 2020, private communication), although further experiments and quantum chemical calculations are needed to confirm this result.

4.2. The Role of NH₂OH in Prebiotic Chemistry

Recent prebiotic experiments conducted under plausible early Earth conditions have shown that NH₂OH is a central species in the synthesis of pyrimidine ribonucleotides (Becker et al. 2019), through its reaction with HC₃N in the presence of urea (NH₂CONH₂). HC₃N is very abundant in G+0.693 (Zeng et al. 2018), and NH₂CONH₂ has also been detected recently toward this source (Jiménez-Serra et al. 2020). Thus, the only missing ingredient was NH₂OH, reported in this paper. Precursors of purine ribonucleotides such as cyanamide (NH₂CN) and glycolaldehyde (CH₂OHCHO) (Powner 2009; Becker et al. 2016), have also been detected in G+0.693 (Requena-Torres et al. 2008; Zeng et al. 2018). Therefore, the G+0.693 molecular cloud presents all precursors of ribonucleotides.

In summary, the detection of NH₂OH in the molecular cloud G+0.693 supports the idea that essential prebiotic precursors of the RNA world could have been synthesized initially in the ISM, to be subsequently transferred to small solar system bodies, and later on to young planets through the impact of meteorites and comets (see e.g., Chyba & Sagan 1992; Pierazzo & Chyba 1999; Pizzarello et al. 2006; Pearce & Pudritz 2015; Martins 2018; Rubin et al. 2019; Rivilla et al. 2020).

We acknowledge the anonymous reviewers for their careful reading of the manuscript and their useful comments. This work is based on observations carried out under projects number 172-18, 018-19, and 133-19 with the IRAM 30 m telescope. IRAM is supported by INSU/CNRS (France), MPG (Germany) and IGN (Spain). We thank the IRAM-30 m staff for the precious help during the different observing runs. V.M.R. acknowledges support from the Comunidad de Madrid through the Atracción de Talento Investigador Senior Grant (COOL: Cosmic Origins Of Life; 2019-T1/TIC-15379), and from the European Union’s Horizon 2020 research and innovation program under the Marie Skłodowska-Curie grant agreement No. 664931. I.J.-S. and J.M.-P. have received partial support from the Spanish FEDER (project number ESP2017-86582-C4-1-R), the Ministry of Science and Innovation through project number PID2019-105552RB-C41, and State Research Agency (AEI) through project number MDM-2017-0737 Unidad de Excelencia María de Maeztu–Centro de Astrobiología (INTA-CSIC).

Appendix A Full Molecular Identification

We list in Table A1 the identified molecular transitions of the molecules that contribute to the spectra shown in Figure 1. We have searched for more than 300 different molecules in our spectral survey, including all the species detected previously toward G+0.693 (e.g., Requena-Torres et al. 2006, 2008; Rivilla et al. 2018, 2019; Zeng et al. 2018; Jiménez-Serra et al. 2020), and those detected so far in the ISM¹³ (McGuire 2018). We show in Table A1 transitions with line intensities $I_L \geq 1$ mK.

¹² <http://kida.astrophy.u-bordeaux.fr>

¹³ See also <https://cdms.astro.uni-koeln.de/classic/molecules>, and http://astrochymist.org/astrochymist_mole.html.

Table A1

Transitions of the Molecules That Contribute to the Spectra Shown in Figure 1

Molecule	Freq. (GHz)	I_L (mK)
3 mm—NH ₂ OH $J = 2-1$		
CH ₃ OCHO	100.6815450	93.3
CH ₃ OCHO	100.6833680	93.4
NH ₂ OH	100.6835800	6.1
CH ₃ OCHO	100.6931270	1.22
HCCCHO	100.7169300	18.4
CH ₃ OCHO	100.734805	1.1
NH ₂ OH	100.7482300	12.1
NH ₂ OH	100.8076200	6.1
CH ₃ COOH	100.8119422	1.52
s-C ₂ H ₅ CHO	100.8149861	6.3
s-C ₂ H ₅ CHO	100.8149861	6.3
2 mm—NH ₂ OH $J = 3-2$		
CH ₃ OCH ₃	150.992109	1.8
CH ₃ OCH ₃	150.9921790	2.8
s-C ₂ H ₅ CHO	150.9952334	1.5
CH ₃ OCH ₃	150.9953910	7.4
s-C ₂ H ₅ CHO	150.9954363	1.5
CH ₃ OCH ₃	150.9954363	1.5
CH ₃ OCH ₃	150.9986390	4.6
NH ₂ OH	151.0207010	11.6
c-C ₃ H ₂	151.0391730	3.2
g-C ₂ H ₅ OH	151.0641006	2.2
s-C ₂ H ₅ CHO	151.0653970	1.1
s-C ₂ H ₅ CHO	151.0654207	1.1
s-C ₂ H ₅ CHO	151.0831633	1.1
s-C ₂ H ₅ CHO	151.0831861	1.1
s-C ₂ H ₅ CHO	151.0970518	1.1
s-C ₂ H ₅ CHO	151.0970740	1.1
NH ₂ OH	151.1019860	2.2
NH ₂ OH	151.1023240	2.2
s-C ₂ H ₅ CHO	151.1148181	1.1
s-C ₂ H ₅ CHO	151.1148394	1.1
NH ₂ OH	151.1176680	19.4
C ₂ H ₅ CN	151.1272640	3.5
HOCH ₂ CN	151.1300319	1.0
CH ₃ COOH	151.1620321	1.5
CH ₃ CHO	151.1671882	18.4
t-HCOOH	151.1762475	81.4
NH ₂ OH	151.2070070	11.6
HCOCH ₂ OH	151.2430164	4.5
1 mm—NH ₂ OH $J = 4-3$		
HDCO	201.3413620	13.2
CH ₃ SH	201.3440150	14.6
NH ₂ OH	201.3525783	13.6
t-C ₂ H ₅ OH	201.4372959	24.3
CH ₃ OH	201.4454903	77.0
NH ₂ OH	201.4606626	3.3
NH ₂ OH	201.4615977	3.3
NH ₂ OH	201.4817175	21.6
NH ₂ OH	201.6007146	13.6
H ₂ C ¹⁸ O	201.6142649	21.4
CH ₃ CONH ₂	201.6210000	1.7

Note. We present the name of the species, the frequency of the transition, and the line intensity I_L .

Appendix B**Detection of Propanal (s-C₂H₅CHO) toward G+0.693**

The syn-conformer of propanal (s-C₂H₅CHO) has been identified toward the G+0.693 molecular cloud. The analysis has been done using the SLIM-MADCUBA tool, following the same procedure described in Section 3. We use the CDMS entry 58505 (version 2018 January). We fixed v_{LSR} to 69 km s⁻¹ and FWHM to 21 km s⁻¹, and obtained $T_{\text{ex}} = 12.0 \pm 0.8$ K, and $N = (7.4 \pm 1.5) \times 10^{13}$ cm⁻², which translates into an abundance with respect to H₂ of $(5 \pm 2) \times 10^{-10}$. The best LTE fit for selected transitions (listed in Table B1) is shown in Figure B1 with a red line. The s-C₂H₅CHO transitions that contribute to the spectra shown in Figure 1 are listed in Table A1.

Table B1Selected Transitions of s-C₂H₅CHO Detected toward G+0.693

Frequency (GHz)	Transition	log A_{ul} (s ⁻¹)	E_u (K)
77.1819857	8 _{1,8} -7 _{1,7} E	-5.1418	17.4
77.1819857	8 _{1,8} -7 _{1,7} A	-5.1418	17.4
77.9521729	8 _{0,8} -7 _{0,7} E	-5.1275	17.3
77.9521729	8 _{0,8} -7 _{0,7} A	-5.1275	17.3
87.0228499	9 _{0,9} -8 _{0,8} E	-4.9808	21.5
87.0228499	9 _{0,9} -8 _{0,8} A	-4.9808	21.5
88.5156329	8 _{2,6} -7 _{2,5} E	-4.9810	21.0
88.5156329	8 _{2,6} -7 _{2,5} A	-4.9810	21.0
88.5476678	3 _{3,1} -2 _{2,0} E	-5.0515	8.0
88.5485859	3 _{3,1} -2 _{2,0} A	-5.0116	8.0
95.2964249	10 _{0,10} -9 _{1,9} E	-4.8656	26.1
95.2964249	10 _{0,10} -9 _{1,9} A	-4.8656	26.1
95.7920583	10 _{1,10} -9 _{1,9} E	-4.8531	26.1
95.7920583	10 _{1,10} -9 _{1,9} A	-4.8531	26.1
96.1200037	10 _{0,10} -9 _{0,9} E	-4.8484	26.1
96.1200037	10 _{0,10} -9 _{0,9} A	-4.8484	26.1
99.3945076	4 _{3,1} -3 _{2,2} E	-4.9654	10.0
99.3945076	4 _{3,1} -3 _{2,2} A	-4.9643	10.0
105.2870083	10 _{1,9} -9 _{1,8} E	-4.7369	29.1
105.2870083	10 _{1,9} -9 _{1,8} A	-4.7369	29.1

Note. We provide the frequencies of the transitions, quantum numbers, the base 10 logarithm of the Einstein coefficients (A_{ul}), and the energy of the upper levels (E_u).

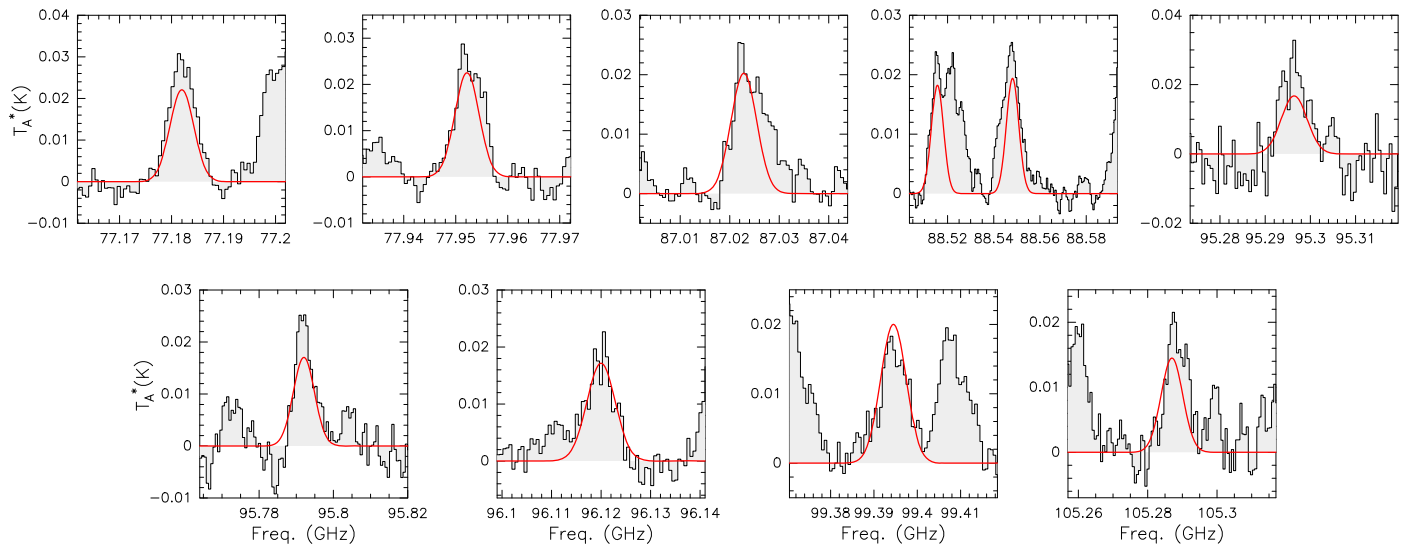


Figure B1. Selected transitions of the syn-conformer of propanal ($s\text{-C}_2\text{H}_5\text{CHO}$) detected toward the G+0.693 molecular cloud (see Table B1). The best LTE fit (see Appendix B) is shown in red.

Appendix C Detections of HNO and N₂O Toward G+0.693

We report here the detection of the nitroxyl radical (HNO) and nitrous oxide (N₂O) toward G+0.693. We show in Figures C1 and C2 the detected transitions of HNO and N₂O,

respectively, which are listed in Table C1. The analysis have been done using the SLIM-MADCUBA tool, following the same procedure described in Section 3. The derived parameters from the fits (N , T_{ex} , FWHM and v_{LSR}) are presented in Table 2.

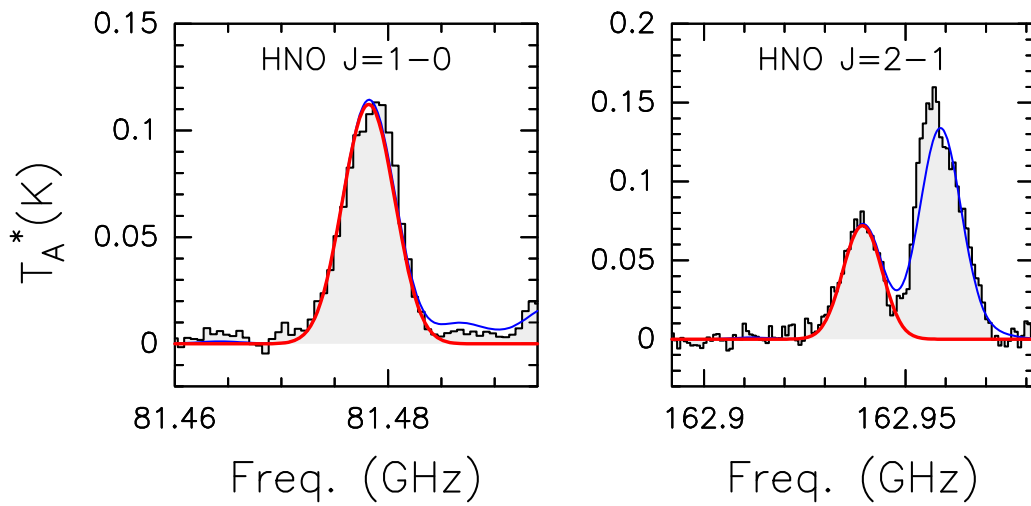


Figure C1. HNO transitions detected toward the G+0.693 molecular cloud. The best LTE fit is shown in red, while the total contribution including other molecular species identified in our spectral survey is shown in blue.

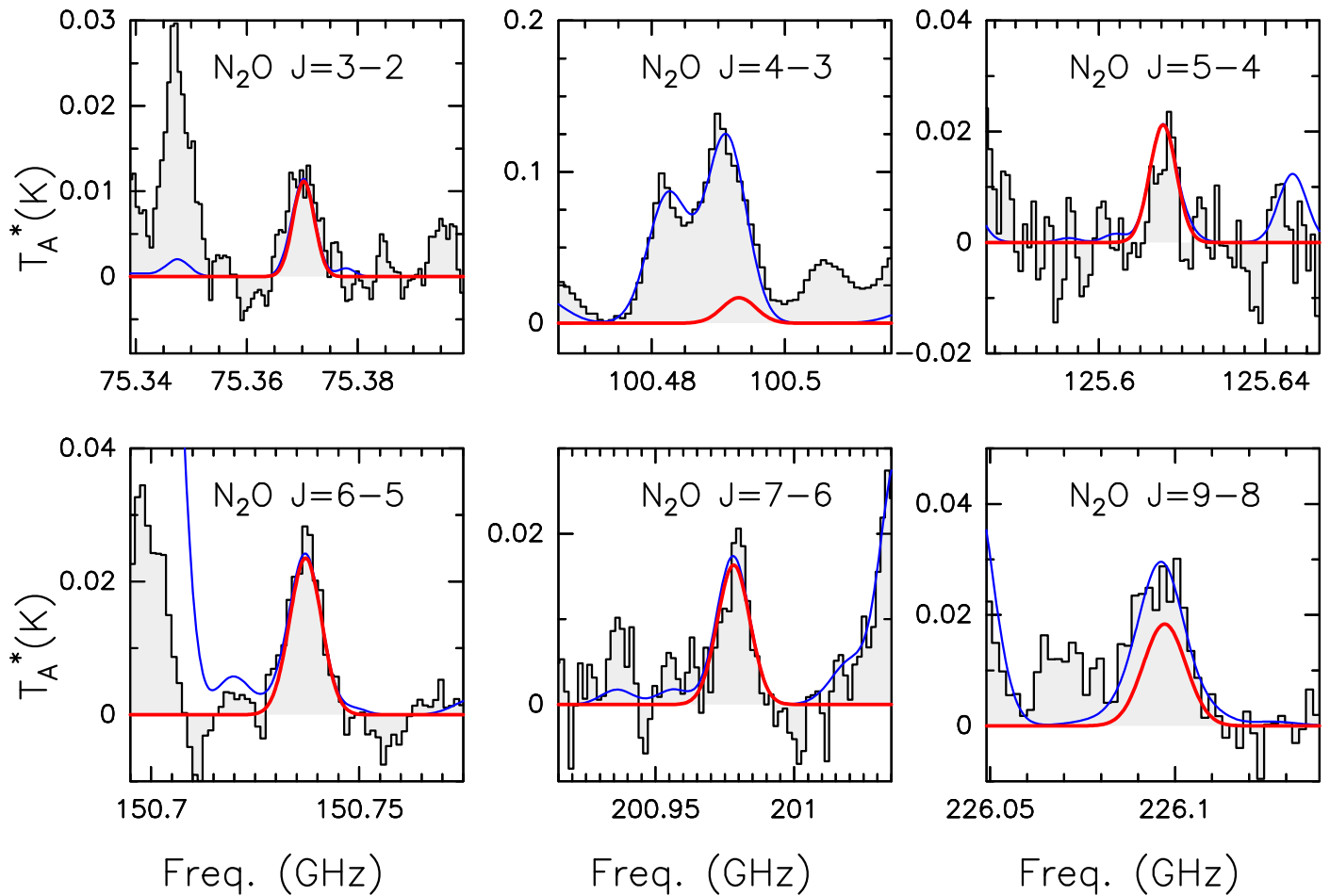


Figure C2. N_2O transitions detected toward the G+0.693 molecular cloud. The best LTE fit is shown in red, while the total contribution including also other molecular species identified in our spectral survey is shown in blue.

Table C1Transitions of HNO (JPL Entry 31005, version 1996 February) and N₂O (JPL entry 44004, version 2014 August) Detected toward G+0.693

Molecule	Frequency (GHz)	Transition ^a	log A _{ul} (s ⁻¹)	E _u (K)
HNO	81.47749	1 _{0,1} -0 _{0,0} F = 2-1	-5.65235	3.9
HNO	81.47749	1 _{0,1} -0 _{0,0} F = 1-1	-5.65240	3.9
HNO	81.47749	1 _{0,1} -0 _{0,0} F = 0-1	-5.65240	3.9
HNO	162.937949	2 _{0,2} -1 _{0,1} F = 3-2	-4.67021	11.7
HNO	162.937949	2 _{0,2} -1 _{0,1} F = 2-1	-4.79519	11.7
HNO	162.937949	2 _{0,2} -1 _{0,1} F = 1-0	-4.92554	11.7
HNO	162.937949	2 _{0,2} -1 _{0,1} F = 1-1	-5.05044	11.7
HNO	162.937949	2 _{0,2} -1 _{0,1} F = 2-2	-5.27229	11.7
HNO	162.937949	2 _{0,2} -1 _{0,1} F = 1-2	-6.22654	11.7
N ₂ O	75.369224	3-2	-7.25771	7.2
N ₂ O ^b	100.49174	4-3	-6.86711	12.1
N ₂ O	125.61369	5-4	-6.56660	18.1
N ₂ O	150.735046	6-5	-6.32247	25.3
N ₂ O	200.975333	8-7	-6.32247	43.4
N ₂ O ^c	226.0940229	9-8	-6.32247	54.3

Notes. We provide the frequencies of the transitions, quantum numbers, the base 10 logarithm of the Einstein coefficients (A_{ul}), and the energy of the upper levels (E_u).

^a The format for the quantum numbers is J_{K_a,K_c} for HNO and J for N₂O.

^b Transition contaminated by CH₃OCHO (100.490682 GHz) and aGg-(CH₂OH)₂ (100.4906121 GHz).

^c Transition contaminated by CH₃SH (226.093108 GHz).

ORCID iDs

Víctor M. Rivilla  <https://orcid.org/0000-0002-2887-5859>

Sergio Martín  <https://orcid.org/0000-0001-9281-2919>

References

- Atkins, J. F., Gesteland, R. F., & Cech, T. R. 2011, in *RNA Worlds: From Life's Origins to Diversity in Gene Regulation*, ed. J. F. Atkins, R. F. Gesteland, & T. R. Cech (Cold Spring Harbor, NY: CSHL Press), 366
- Becker, S., Feldmann, J., Wiedemann, S., et al. 2019, *Sci*, **366**, 76
- Becker, S., Thoma, I., Deutsch, A., et al. 2016, *Sci*, **352**, 833
- Belloche, A., Garrod, R. T., Müller, H. S. P., et al. 2019, *A&A*, **628**, A10
- Belloche, A., Müller, H. S. P., Menten, K. M., Schilke, P., & Comito, C. 2013, *A&A*, **559**, A47
- Blagojevic, V., Petrie, S., & Bohme, D. K. 2003, *MNRAS*, **339**, L7
- Charnley, S. B., Rodgers, S. D., & Ehrenfreund, P. 2001, *A&A*, **378**, 1024
- Chyba, C., & Sagan, C. 1992, *Natur*, **355**, 125
- Codella, C., Viti, S., Lefloch, B., et al. 2018, *MNRAS*, **474**, 5694
- Congiu, E., Fedoseev, G., Ioppolo, S., et al. 2012, *ApJL*, **750**, L12
- Endres, C. P., Schlemmer, S., Schilke, P., Stutzki, J., & Müller, H. S. P. 2016, *JMoSp*, **327**, 95
- Fedoseev, G., Ioppolo, S., Lamberts, T., et al. 2012, *JChPh*, **137**, 054714
- Garrod, R. T. 2013, *ApJ*, **765**, 60
- Garrod, R. T., Widicus Weaver, S. L., & Herbst, E. 2008, *ApJ*, **682**, 283
- Gilbert, W. 1986, *Natur*, **319**, 618
- Ginsburg, A., Henkel, C., Ao, Y., et al. 2016, *A&A*, **586**, A50
- Halfen, D. T., Apponi, A. J., & Ziurys, L. M. 2001, *ApJ*, **561**, 244
- Hasegawa, T. I., Herbst, E., & Leung, C. M. 1992, *ApJS*, **82**, 167
- He, J., Vidalí, G., Lemaire, J.-L., & Garrod, R. T. 2015, *ApJ*, **799**, 49
- Hollis, J. M., Lovas, F. J., & Jewell, P. R. 2000, *ApJL*, **540**, L107
- Hüettemeister, S., Wilson, T. L., Bania, T. M., & Martín-Pintado, J. 1993, *A&A*, **280**, 255
- Jiménez-Serra, I., Martín-Pintado, J., Rivilla, V. M., et al. 2020, *AsBio*, in press (doi:10.1089/ast.2019.2125)
- Jørgensen, J. K., van der Wiel, M. H. D., Coutens, A., et al. 2016, *A&A*, **595**, A117
- Krieger, N., Ott, J., Beuther, H., et al. 2017, *ApJ*, **850**, 77
- Ligterink, N. F. W., Calcutt, H., Coutens, A., et al. 2018, *A&A*, **619**, A28
- Martín, S., Martín-Pintado, J., Blanco-Sánchez, C., et al. 2019, *A&A*, **631**, A159
- Martín, S., Requena-Torres, M. A., Martín-Pintado, J., & Mauersberger, R. 2008, *ApJ*, **678**, 245
- Martins, Z. 2018, *Life*, **8**, 28
- McGuire, B. A. 2018, *ApJS*, **239**, 17
- McGuire, B. A., Carroll, P. B., Dollhopf, N. M., et al. 2015, *ApJ*, **812**, 76
- Mojzsis, S. J., Arrhenius, G., McKeegan, K. D., et al. 1996, *Natur*, **384**, 55
- Morino, I., Yamada, K., Klein, H., et al. 2000, *JMoSt*, **517-518**, 367
- Nishi, N., Shinohara, H., & Okuyama, T. 1984, *JChPh*, **80**, 3898
- Patel, B. H. P. C. R. D. J. D. C. D. S. J. D. 2015, *NatCh*, **7**, 301
- Pearce, B. K. D., & Pudritz, R. E. 2015, *ApJ*, **807**, 85
- Pickett, H. M., Poynter, R. L., Cohen, E. A., et al. 1998, *JQSRT*, **60**, 883
- Pierazzo, E., & Chyba, C. F. 1999, *M&PS*, **34**, 909
- Pizzarello, S., Cooper, G. W., & Flynn, G. J. 2006, in *The Nature and Distribution of the Organic Material in Carbonaceous Chondrites and Interplanetary Dust Particles*, ed. D. S. Lauretta & H. Y. McSween (Tucson, AZ: Univ. Arizona Press), 625
- Powner, M. W. G. B. S. J. D. 2009, *Natur*, **459**, 239
- Pullian, R. L., McGuire, B. A., & Remijan, A. J. 2012, *ApJ*, **751**, 1
- Requena-Torres, M. A., Martín-Pintado, J., Martín, S., & Morris, M. R. 2008, *ApJ*, **672**, 352
- Requena-Torres, M. A., Martín-Pintado, J., Rodríguez-Franco, A., et al. 2006, *A&A*, **455**, 971
- Rivilla, V. M., Drozdovskaya, M. N., Altwegg, K., et al. 2020, *MNRAS*, **492**, 1180
- Rivilla, V. M., Jiménez-Serra, I., Zeng, S., et al. 2018, *MNRAS*, **475**, 30
- Rivilla, V. M., Martín-Pintado, J., Jiménez-Serra, I., et al. 2019, *MNRAS*, **483**, L114
- Rodríguez-Fernández, N. J., Martín-Pintado, J., Fuente, A., & Wilson, T. L. 2004, *A&A*, **427**, 217
- Rubin, M., Bekaert, D. V., Broadley, M. W., Drozdovskaya, M. N., & Wampfler, S. F. 2019, *ESC*, **3**, 1792
- Ruiz-Mirazo, K., Briones, C., & de la Escosura, A. 2014, *ChRv*, **114**, 285
- Tsegaw, Y. A., Góbi, S., Förstel, M., et al. 2017, *JPCA*, **121**, 7477
- Tsunekawa, S. 1972, *JPSJ*, **33**, 167
- Turner, B. E. 1971, *ApJL*, **163**, L35
- Turner, B. E., Liszt, H. S., Kaifu, N., & Kisliakov, A. G. 1975, *ApJL*, **201**, L149
- Wakelam, V., Herbst, E., Loison, J.-C., et al. 2012, *ApJS*, **199**, 21
- Zeng, S., Jiménez-Serra, I., Rivilla, V. M., et al. 2018, *MNRAS*, **478**, 2962
- Zheng, W., & Kaiser, R. I. 2010, *JPCA*, **114**, 5251
- Ziurys, L. M., Apponi, A. J., Hollis, J. M., & Snyder, L. E. 1994, *ApJL*, **436**, L181